Teleseismic S-wave microseisms

Kiwamu Nishida,[1*] and Ryota Takagi[2]

[1]Earthquake Research Institute, University of Tokyo,

1-1-1 Yayoi 1, Bunkyo-ku, Tokyo 113-0032, Japan

[2] Research Center for Prediction of Earthquakes and Volcanic Eruptions,

Graduate School of Science, Tohoku University

6-6 Aza-Aoba, Aramaki, Aoba-ku, Sendai 980-8578, Japan

*To whom correspondence should be addressed; E-mail: knishida@eri.u-tokyo.ac.jp.

Although observations of microseisms excited by ocean swells were firmly established in the 1940s, the source locations remain difficult to track. Delineation of the source locations and energy partition of the seismic wave components are key to understanding the excitation mechanisms. Here we report an observation of both P- and S-wave microseisms excited by a severe distant storm in the Atlantic Ocean using a seismic array in Japan. Although nonlinear forcing of an ocean swell with a 1-D Earth model can explain P-waves and vertically polarized S-waves (SV-waves), it cannot explain horizontally polarized S-waves (SH-waves). The precise source locations may provide a new catalog for exploring the Earth's interior.

One Sentence Summary: Precise source locations of teleseismic P- and S-wave microseisms may provide a new catalog for exploring the Earth's interior.

Microseisms are ambient seismic wavefields (*1*) that occur in the 0.05–0.5 Hz frequency range. Although they had been recognized as ambient noise for seismic observation, a new technique known as seismic interferometry turned them into signals for exploring Earth's interior (*2*). They can be categorized into two groups according to the typical frequencies. The first group is classified as primary microseisms ranging 0.05–0.1 Hz, which corresponds to the typical frequency of ocean swells. The second is classified as secondary microseisms ranging 0.1–0.5 Hz, which doubles the frequency of an ocean swell, indicating that the secondary

microseisms are generated through nonlinear wave-wave interactions (*3, 4*). They excite surface waves dominantly.

P-wave microseisms from distant storms have been studied (*5, 6*) by array analysis of dense seismic data. Source locations of the P-wave provided a better spatial localization of the excitation source than that of surface waves. The estimated source distribution was consistent with a theoretical estimation using wave action models. Most studies have focused, however, only on P-waves recorded as vertical components because of the larger amplitudes. Although S-wave amplitudes are estimated to be one order of magnitude smaller than P-wave ones (*7, 8*), the precise locations of P- and S-waves can help in understanding the excitation mechanism.

The energy partition between Love and Rayleigh waves is also another key parameter for understanding the force system of excitation sources. The force system can be characterized by the surface pressure source and/or shear traction on the seafloor (*9*). The observed dominance of Love waves in primary microseisms suggests that they are generated by pressure loadings of an ocean swell acting on a sloping coast (*10*). However, the scattering of surface waves during propagation distorts the energy ratio at the source area. Because the teleseismic body waves are less scattered, the energy partition between P- and S-waves is more appropriate for understanding the source mechanism. However, the smaller body-wave amplitudes at a distance tend to be masked by the surface waves due to local ocean swell activities (*8, 11, 12*).

For the detection of both P- and S-wave microseisms, we conducted an array analysis using 202 Hi-net stations operated by NIED in Chugoku district, where the crustal heterogeneity is weak in Japan (Fig. 1A). NIED deployed 3-component velocity-meters with natural frequency of 1 Hz at the bottom of a borehole of each station. We deconvolved the instrumental response using the inverse filtering technique (*13*) after the reduction of common logger noise (*14*) to utilize low frequency components below 1 Hz. We analyzed data of a rapidly deepening cyclonic low-pressure area known as a "*weather bomb*" (*15*) with a central pressure of about 940 hPa that developed in the Atlantic between Iceland and Greenland on December 9–11, 2014 (*16*). The system was a typical explosive cyclogenesis with a reduction of 24 hPa in 24h on December 9. We divided the records into 1024 s segments. After the exclusion of noisy data, we calculated two-dimensional frequency–slowness spectra (*9*) in the 0.1–0.2 Hz frequency window (Fig. 1B) assuming that signals at a station can be represented by a superposition of plane waves. The spectrum at a certain slowness vector represents the sum of all the records with the predicted time delays. The spectra have local maxima in the slowness domain, where signals recorded at all the stations are in phase.

The spectra of the vertical and radial components displayed a clear teleseismic P-wave. The slowness of about 0.05 [s/km] and the back azimuth of -5 degree were consistent with that of a P-wave traveled from the Atlantic Ocean. The dominant P-wave can be explained by the nonlinear forcing by ocean swell (*7*) based on the Longuet-Higgins's theory (*3*), which can be represented by a vertical single force on the sea surface equivalently.

The spectrum of the radial component showed not only a P-wave but also a rarely seen SV-wave (*8*) with mean square (MS) amplitude of about 8% of the P-wave amplitude. The observed slowness of the SV wave suggests that the source could be located in the same area of

the P-wave microseisms in the Atlantic Ocean. The simplest mechanism of the observed S-wave excitation is the P to SV conversion on the sea bottom during multiple reflections within the ocean (*7*). Although the theoretical MS amplitude (*7*) of an SV-wave is two orders smaller than that of a P-wave, the amplitude depends strongly on the incident angle. Within the possible range based on different 1-D seismic velocity models, our observation is consistent with the prediction.

Surprisingly, the spectrum of the transverse component also showed an SH-wave microseism. A pressure source in the ocean cannot excite the SH-waves in a spherically stratified Earth. Therefore, the shear traction acting on the sea-bottom horizon is required. This observation suggests that the steep topography beneath the source and thick sediments may affect the excitation. The smaller recorded amplitude of about 3% of the P-wave MS amplitude (Fig. 3) suggests that this effect is secondary.

We inferred the centroid locations of P-wave microseisms by a method which is similar to the GRiDMT technique (*21*) as follows. We modeled the localized excitation source by approximating the source using a vertical single force at a surface point. We characterized the source by the centroid location and the root mean square amplitude (RMS) of the single force. We justify the point source approximation as the localized source area was on the order of 10^5 km^2, which we estimated by using the wave model WAVEWATCH III (*17, 18*)(Fig. S1) and is smaller than the array response function (Fig. 1A). At an assumed grid point, RMS of the vertical single force was estimated by modeling the seismic wave fields using a ray-theory P-wave Green's function (*19*) for a 1-D Earth model (*20*). The variance reductions between the modeled wave field and the observations were calculated at assumed grid points every $0.1^\circ \times 0.1^\circ$ in longitude and latitude. The maximum was selected as the centroid location for the vertical single force. We subtracted the station correction terms using a multichannel cross-correlation method (*22*) with an earthquake occurred close to Iceland on August 30, 2012 (Fig. 1A) as 3-D seismic structure biases the locations of the centroids. Without the station corrections, the centroid of the earthquake located by this method deviated about 300-km away from the original location. Orange dots in Fig. 2A represent the locations of the centroids inferred from the vertical components at 775 stations. RMSs of the centroid single force were on the order of 10^{11} N (Fig. 2D). They were consistent with the theoretical estimation of the wave model (Fig. S2) and a previous study (*12*). The inferred centroid locations were consistent with a theoretical model (Fig. S1). The centroids migrated along an area that contains a strong site effect (*7*) of the ocean layer. This can be described as the constructive interference of multiply reflected P-waves in the ocean that are converted to P- and SV-waves at the sea bottom (*7*). The site effect becomes larger where the resonance frequency of the oceanic layer matches the P-wave frequency. From time period (i) to (ii) shown in Fig. 2A, the centroids migrated along the strong site effect area. From (ii) to (iv), they were not in the area. From (iv) to (v), they migrated along the area again. We can explain this observation from (ii) to (iv) by the larger source area (Fig. S1) including both the part from (i) to (ii) and that from (iv) to (v) in Fig. 2A with the strong site effects. This method determined the centroids of the distributed sources with weighting by the site effects.

We located centroids of the SH- and SV-waves by back-projecting the seismograms in the horizontal components with the station corrections (*24*). We did not estimate the equivalent single force, because modelling is not practical due to the near source amplification from multiple reflections in the ocean and sedimentary layers. The centroid locations of the SH- and SV-waves are shown with a resonant frequency of the sediment (*19*) (Fig. 2A) that corresponds to the fundamental mode in a close pipe system, based on the CRUST1.0 (*25*). Our centroid locations of the SV-waves were close to the P-wave centroids. However, our centroid locations of the SH-waves were to the west (in particular at around (iii) as shown in Fig. 2C), where the sediments have lower resonant frequencies closer to the SH-wave frequency as we observed in Fig. 2B. Our observation suggests SH-waves trapped in the sedimentary layer. Moreover, the peak frequency of the SH-wave at 0.13 Hz was similar to those of the P- and SV-waves (Fig. 3). We suggested the transfer of a large part of the SV-wave energy into the sediments from the P-wave to explain the frequency overlap, where the sedimentary resonant frequency matched the dominant frequency of the P-wave microseisms. During multiple reflections of the SV-wave in the sediment, the polarization information was lost and part of the SV-wave energy was converted to the SH-wave over time (*19*).

Body-wave microseisms provide information about the Earth's deep interior beneath the stations via seismic interferometry (*26*), which extracts seismic-wave propagation between station pairs. We have characterized the excitation source by a centroid vertical single force (*3, 4, 7*). Hence, the seismic structure beneath a storm can be explored using body-wave microseisms. Because the estimated vertical single force is consistent with a former study (*12*), we can expect similar potential events with amplitude on the order of 10^{11} N. A collection of precise locations of the centroid single force may provide a catalog for exploring the Earth's interior. Such a catalog may open a different perspective to explore the Earth's deep interior beneath a storm in the absence of seismic stations and earthquakes.

References and Notes

1. B. Gutenberg, Microseisms and weather forecasting, *J. Atmos. Sci.* **4**, 21 (1947).

2. R. Snieder, E. Larose,(2013). Extracting Earth ' s Elastic Wave Response from Noise Measurements, *Annu. Rev. Earth Planet. Sci.* **41**, 183–206 (2013).

3. M. S. Longuet-Higgins, A Theory of the Origin of Microseisms, *Phil. Trans. Roy. Soc. A* **243**, 1–35 (1950).

4. S. Kedar, M. Longuet-Higgins, F. Webb, N. Graham, R. Clayton, C. Jones, The origin of deep ocean microseisms in the North Atlantic Ocean, *Proc. Roy. Soc. A* **464**, 777–793 (2008).

5. P. Gerstoft, M. C. Fehler, K. G. Sabra, When Katrina hit California, *Geophys. Res. Lett.* **33**, L17308 (2006).

6. M. Landès, F. Hubans, N. M. Shapiro, A. Paul, M. Campillo, Origin of deep ocean microseisms by using teleseismic body waves, *J. Geophys. Res.* **115**, B05302 (2010).

7. L. Gualtieri, E. Stutzmann, V. Farra, Y. Capdeville, M. Schimmel, F. Ardhuin, A. Morelli, Modelling the ocean site effect on seismic noise body waves, *Geophys. J. Int.* **197**, 1096–1106 (2014).

8. Q. Liu, K. Koper, R. Burlacu, S. Ni, F. Wang, C. Zou, A.—Reading, Source locations of teleseismic P, SV, and SH waves observed in microseisms recorded by a large aperture seismic array in China. *Earth Planet. Sci. Let.* **449**, 39–47 (2016).

9. K. Nishida, H. Kawakatsu, Y. Fukao, K. Obara, Background Love and Rayleigh waves simultaneously generated at the Pacific Ocean floors, *Geophys. Res. Lett.* **35**, L16307 (2008).

10. F. Ardhuin, L. Gualtieri, E. Stutzmann, How ocean waves rock the Earth: Two mechanisms explain microseisms with periods 3 to 300 s, *Geophys. Res. Lett.* **42**, 765–772 (2015).

11. M. N. Toksöz, R. T. Lacoss, Microseisms: Mode Structure and Sources, *Science* **159**, 872–873 (1968).

12. L. Vinnik, Sources of microseismicP waves, *Pure Appl. Geophys.* **103**, 282–289 (1973).

13. T. Maeda, K. Obara, T. Furumura, T. Saito, Interference of long-period seismic wavefield observed by the dense Hi-net array in Japan, *J. Geophys. Res.* **116**, B10303 (2011).

14. R. Takagi, K. Nishida, Y. Aoki, T. Maeda, K. Masuda, M. Takeo, K. Obara, K. Shiomi, M. Sato, K. Saito, A Single Bit Matters: Coherent Noise of Seismic Data Loggers, *Seismological Res. Lett.* **86**, 901–907 (2015).

15. T. Matsuzawa, K. Obara, T. Maeda, Y. Asano, T. Saito, Love- and Rayleigh-Wave Microseisms Excited by Migrating Ocean Swells in the North Atlantic Detected in Japan and Germany, *Bull. Seism. Soc. Am.* **102**, 1864–1871 (2012).

16. *Weather* **70**, 54 (2015).

17. H.L. Tolman, A mosaic approach to wind wave modeling, *Ocean Modelling* **25**, 35–47 (2008).

18. F. Ardhuin, E. Stutzmann, M. Schimmel, A. Mangeney, Ocean wave sources of seismic noise, *J. Geophys. Res.* **116**, 1–21 (2011).

19. Materials and Methods are available as Supplementary Materials on Science Online.

20. B. L. N. Kennett, E. R. Engdah, R. Buland, Constraints on seismic velocities in the Earth from traveltimes, *Geophys. J. Int* **122**, 108–124 (1995).

21. H. Kawakatsu, On the realtime monitoring of the long-period seismic wavefield, *Bull. Earth. Res. Inst.* **73**, 267–274 (1998).

22. J. VanDecar, R. S. Crosson, B. Y. J. C. Vandecar, R. S. Crosson, Determination of teleseismic relative phase arrival times using multi-channel cross-correlation and least squares, *Bull. Seismol. Soc. Am.* **80**, 150–169 (1990).

23. B. Efron, Bootstrap methods: Another look at the jackknife, *Ann. Stat.* **7**, 1–26 (1979).

24. M. Ishii, P. M. Shearer, H. Houston, J. E. Vidale, Extent, duration and speed of the 2004 Sumatra-Andaman earthquake imaged by the Hi-Net array, *Nature* **435**, 933-936 (2005).

25. G. Laske, G. Masters, Z. Ma, M. Pasyanos, Update on CRUST1.0 - A 1-degree Global Model of Earth's Crust, *EGU General Assembly Conference Abstracts* (2013), vol. 15 of *EGU General Assembly Conference Abstracts*, pp. EGU2013–2658.

26. P. Poli, M. Campillo, H. Pedersen, Body-Wave Imaging of Earth's Mantle Discontinuities from Ambient Seismic Noise, *Science* **338**, 1063-1065 (2012).

Acknowledgments:

We thank S. Kedar, an anonymous reviewer, and E. Stutzmann for constructive comments. Hi-net seismic records were provided by NIED at http://www.hinet.bosai.go.jp. This work was supported by JSPS KAKENHI Grant Numbers 26400448 and 15J11322.

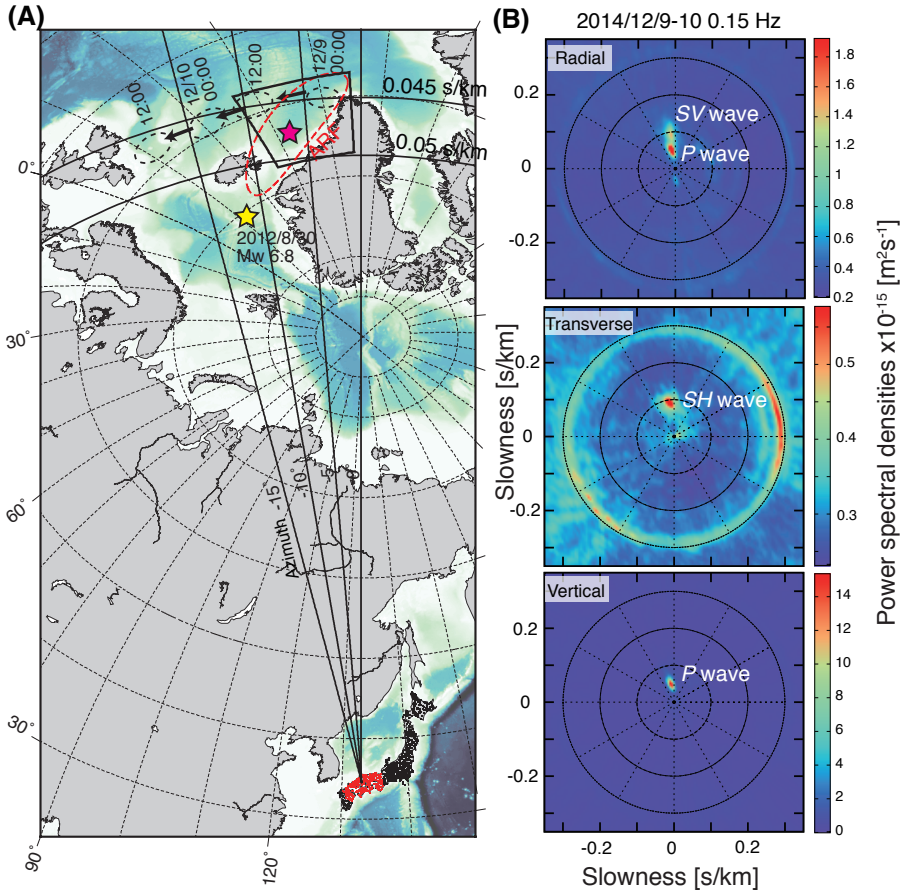

Figure 1: Rough source location (the red star) estimated by backprojection of the observed body-wave microseisms. (A) Station distribution and location of the ”weather bomb”. Red points in Japan indicate the station locations used in the slowness–frequency analysis. Black and red dots show all the Hi-net station locations. The red dashed line represents 0.5 of the array response function for a point source at (-32.5, 63) shown by the red star. The trapezoid region indicates the area shown in Fig. 2A. The location of the earthquake is indicated by the star symbol. (B) Frequency–slowness spectra of radial, transverse, and vertical components at 0.15 Hz. This figure shows the P-wave traveling from the north direction with back azimuth of about $-7°$. The slowness is about 0.48 s/km, which determined the distance between the source and the receivers as shown in Fig. 1A.

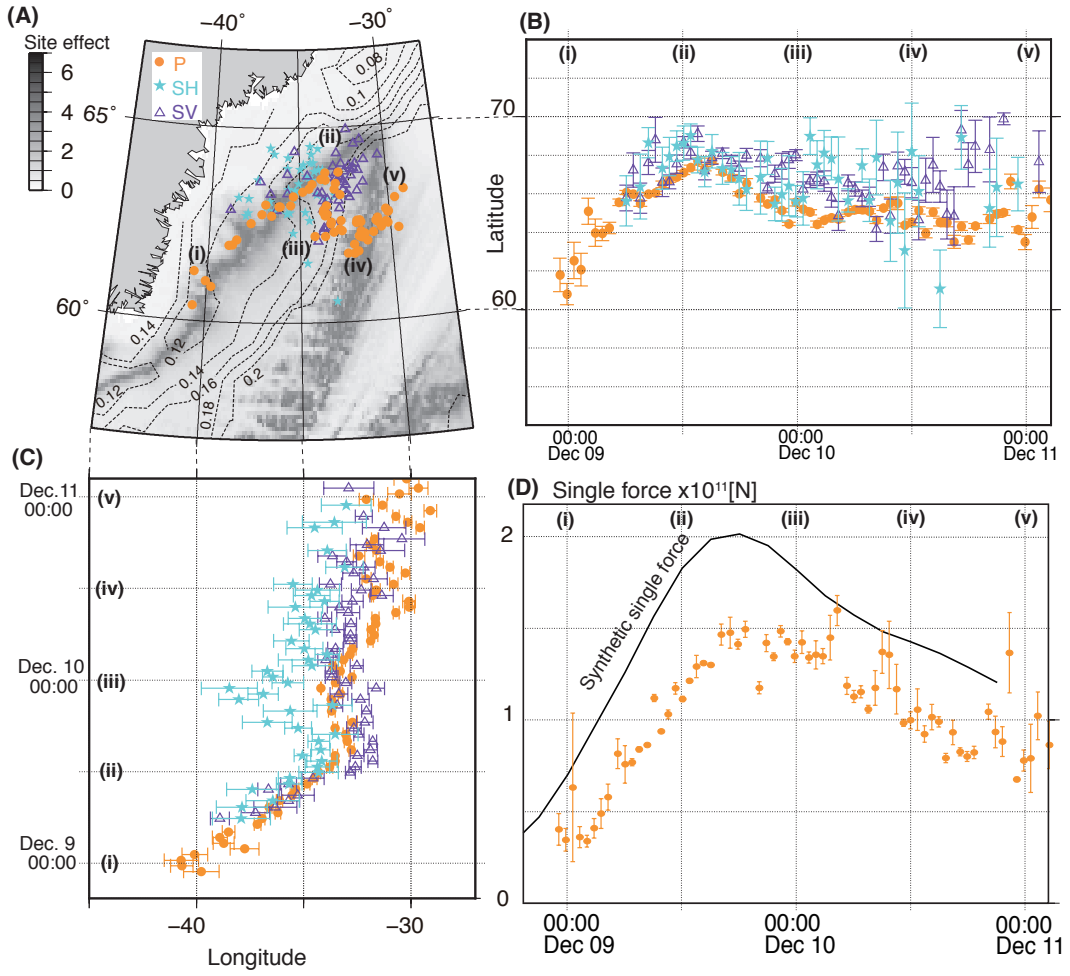

Figure 2: Migration of precise centroid locations of P, SV, and SH waves. (A) Locations of the centroids with errors smaller than 1.5° in latitude and longitude. The error was estimated by the bootstrap method (*23*). Orange dots indicate the centroids of the P-wave microseisms. Purple triangles indicate the SV-waves. Blue stars indicate the SH-wave. The background image shows the site effect of the ocean layer, whereas the contours show the resonant frequency of the sediment. The resonant frequency was estimated by a four-way travel time of multiple reflection of sediment-derived S-waves in the vertical direction. (i)-(v) represent time labels every 12 h as shown in Fig. 2B. (B) Latitude of centroids of P-, SH-, and SV-waves with respect to time.(C) Longitude of the centroids with respect to time. This figure shows that source locations of SH wave at 0h on Dec. 10 were west to the others. (D) Temporal variations of root mean square amplitudes of the single force. The black line shows a synthetic vertical single force (*19*).

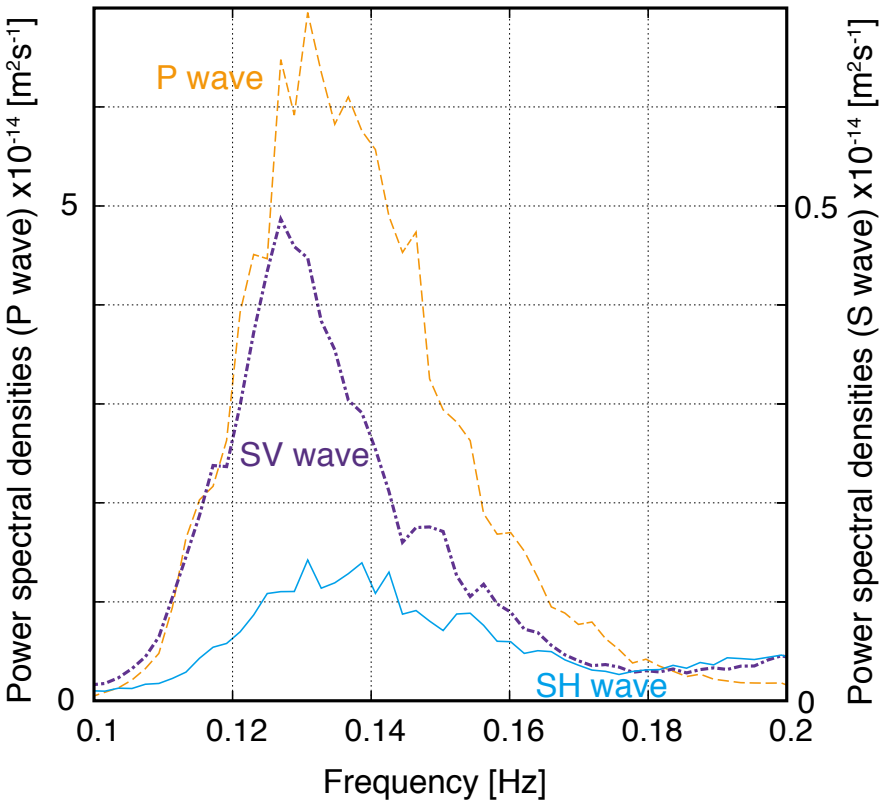

Figure 3: Stacked power spectra of P- (orange dashed line), SV- (black dashed-dotted line), and SH-waves (blue line). They are power spectra of the seismograms of vertical (P wave), radial (SV wave) and transverse components (SH wave) with shift in time according to the corresponding travel times for the located centroids from December 9 to 11, 2014. The power spectral densities of the SV-waves were 8% of the P-wave. The SH-waves consisted of one third of those for the SV-waves. The peak frequencies of P-, SV-, and SH-waves were about 0.13 Hz.

Materials and Methods
Figs. S1 to S3
References (27–31)